



CHARACTERISTICS OF BOUNDARY LAYER FLOW INDUCED BY SOLITARY WAVE PROPAGATING OVER HORIZONTAL BOTTOM

Chang Lin

Department of Civil Engineering, National Chung Hsing University, Taichung, Taiwan, R.O.C.

Shi-Min Yu

Department of Civil Engineering, National Chung Hsing University, Taichung, Taiwan, R.O.C.

Po-Hung Yeh

Department of Civil Engineering, National Chung Hsing University, Taichung, Taiwan, R.O.C.

Min-Hsuan Yu

Department of Civil Engineering, National Chung Hsing University, Taichung, Taiwan, R.O.C.

Ching-Piao Tsai

Department of Civil Engineering, National Chung Hsing University, Taichung, Taiwan, R.O.C., cptsai@nchu.edu.tw

See next page for additional authors

Follow this and additional works at: <https://jmstt.ntou.edu.tw/journal>



Part of the [Engineering Commons](#)

Recommended Citation

Lin, Chang; Yu, Shi-Min; Yeh, Po-Hung; Yu, Min-Hsuan; Tsai, Ching-Piao; Hsieh, Shih-Chun; Kao, Ming-Jer; Tzeng, Guang-Wei; and Raikar, Rajkumar (2015) "CHARACTERISTICS OF BOUNDARY LAYER FLOW INDUCED BY SOLITARY WAVE PROPAGATING OVER HORIZONTAL BOTTOM," *Journal of Marine Science and Technology*: Vol. 23: Iss. 6, Article 10.

DOI: 10.6119/JMST-015-0610-9

Available at: <https://jmstt.ntou.edu.tw/journal/vol23/iss6/10>

This Research Article is brought to you for free and open access by Journal of Marine Science and Technology. It has been accepted for inclusion in Journal of Marine Science and Technology by an authorized editor of Journal of Marine Science and Technology.

CHARACTERISTICS OF BOUNDARY LAYER FLOW INDUCED BY SOLITARY WAVE PROPAGATING OVER HORIZONTAL BOTTOM

Acknowledgements

This work was performed under the support of National Science Council, Taiwan (Grant No. NSC 99-2221-E-005-117- MY3). The authors would like to express their sincere appreciation to UTOPIA Instruments Co., Ltd. for helping the test of high-speed digital camera.

Authors

Chang Lin, Shi-Min Yu, Po-Hung Yeh, Min-Hsuan Yu, Ching-Piao Tsai, Shih-Chun Hsieh, Ming-Jer Kao, Guang-Wei Tzeng, and Rajkumar Raikar

CHARACTERISTICS OF BOUNDARY LAYER FLOW INDUCED BY SOLITARY WAVE PROPAGATING OVER HORIZONTAL BOTTOM

Chang Lin¹, Shi-Min Yu¹, Po-Hung Yeh¹, Min-Hsuan Yu¹, Ching-Piao Tsai¹,
Shih-Chun Hsieh¹, Ming-Jer Kao¹, Guang-Wei Tzeng¹, and Rajkumar Raikar²

Key words: bottom boundary layer, solitary wave, high-speed particle image velocimetry (HSPIV), similarity profile.

ABSTRACT

Experimental results on the flow characteristics of bottom boundary layer induced by a solitary wave propagating over a horizontal bottom are presented. Particle-trajectory flow visualization technique and high-speed particle image velocimetry (HSPIV) were used to elucidate detailed velocity fields underneath solitary waves with the ratios of wave height to water depth from 0.130 to 0.386. The results show that the velocity profiles can be classified into two classes with respect to the passage of the solitary wave-crest at the measuring section: *the pre-passing* and *post-passing phases*. For the pre-passing phase, the velocity distributions can be deduced to a unique similarity profile with the use of unsteady free stream velocity and time-dependent boundary layer thickness as the characteristic velocity and length scales. On the other hand, the similarity profile for the flow reversal, acting like an unsteady wall jet, is obtained from the velocity distributions during the post-passing phase. The velocity deficit between the unsteady free stream velocity and the maximum negative velocity as well as the (time-dependent) thickness of reversal flow were identified as the characteristic velocity and length scales, respectively.

I. INTRODUCTION

As a solitary wave transverses the ocean and reaches the nearshore region, the influence from sea bed becomes more profound because of the shallow water depth. Bottom friction,

the consequential momentum exchange, and energy dissipation are all intensified within the very thin bottom boundary layer. Changes in wave shape and celerity are anticipated and have been reported by many investigations and studies. Research of the boundary layer flow under a solitary wave has been largely progressed since Keulegan (1948), in which the analytical equations dealing with damping by viscous effects of solitary waves was derived. Ott and Sudan (1970) modified the KdV (Korteweg-de Vries) equation to include energy dissipation. A linear dissipation rate was added in the equation. Mei (1983) used perturbation method to re-derive analytical equations. Similar results with Keulegan's (1948) were obtained. Liu and Orfila (2004) published a milestone paper in which sets of Boussinesq-type depth-integrated equations for long-wave propagation were derived. The equations include viscous effects and are able to estimate the damping rates for both harmonic progressive waves and a solitary wave. Liu et al. (2006) further extended Liu and Orfila's (2004) formulation from constant depth to slowly varying depth. Few experiments were carried out in the laboratory to validate the resulting formulation, with tests of solitary wave damping and shoaling. Good agreement was found between the numerical results and the experimental data. In addition, bottom shear stress was also derived in the study and compared with conventional empirical model. The effects of turbulent bottom boundary layer were included in the formulation of Liu and Orfila (2004) by Liu et al. (2006). The eddy viscosity in the turbulence closure model was assumed to be a power function of the vertical elevation. Phase shift between the bottom stress and the depth-averaged velocity for simple harmonic progressive waves, and the damping rate of a solitary wave were both derived.

The laminar boundary layer flow under a solitary wave was particularly examined in Liu et al. (2007). It is found that the negative velocity inside laminar boundary layer and the reverse direction of bed shear stress occur when the solitary wave is decelerating. Very few laboratory measurements were conducted to check the theoretical results. In addition, Sumer et al. (2010) studied the boundary layer flow under solitary

Paper submitted 11/29/14; revised 01/28/15; accepted 06/10/15. Author for correspondence: Ching-Piao Tsai (e-mail: cptsai@nchu.edu.tw).

¹ Department of Civil Engineering, National Chung Hsing University, Taichung, Taiwan, R.O.C.

² Department of Civil Engineering, K. L. E. S. College of Engineering and Technology, Belgaum.

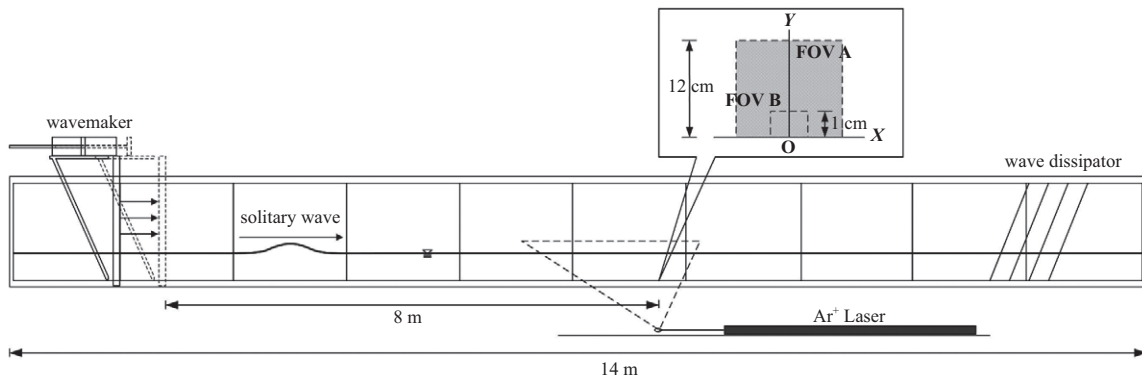


Fig. 1. Schematic sketch of experimental setup.

motion by using laser Doppler velocimetry (LDV) and hot film probe. Prescribed free-stream velocity outside the bottom boundary layer was simulated in a large U-tube to investigate the bottom boundary layer and bed shear stress. Flow visualization employing a thin-layered milk tracer was also performed to help identify the flow characteristics in different flow regimes. The developments of non-intrusive measurement techniques, such as LDV and particle image velocimetry (PIV) have provided more accurate measurements for the boundary layer flow studies. Many applications can be seen in the studies of laminar and turbulent boundary layer flows of progressive, standing, or solitary waves, e.g. Sleath (1987); Jensen et al. (1989); Lin et al. (2002a-c); Carstensen et al. (2010) and Sumer et al. (2010). Although LDV has the advantages such like higher spatial and velocity resolution, no calibration required, and measuring very near boundaries without biases, its point-measurement nature creates measurement uncertainties and thus hinders its application to some topics. On the other hand, PIV provides a whole view velocity measurement, largely reducing the ensemble error required by the point-measurement algorithm. Moreover, following the rapid development of optical apparatus and technologies, the image grabbing tool has transformed from traditional film cameras to high-speed video cameras. High time-resolved PIV makes the boundary layer flow measurement more accurate and has become the main stream in the research community, e.g. Liu et al. (2007) and Lin et al. (2014a, b).

The present study is an attempt to examine the characteristics of boundary flow under a solitary wave propagating over a horizontal bottom. Physical modeling in laboratory was conducted and delicate experiments were performed, using particle-trajectory flow visualization technique and high-time resolved PIV measurements. The use of PIV was aimed to obtain instantaneous velocity fields inside the bottom boundary layer. Due to the limitation of wave flume used, the flow conditions were set in the laminar flow regime. The evolution of the boundary layer thickness is first explored and elucidated. Some similarity profiles of the horizontal velocity in the laminar boundary layer were emphasized. Nonlinear regression analyses were then performed on the results. Selec-

tion of suitable characteristic velocity and length scales amongst various alternatives was studied to derive similarity profiles in the bottom boundary layer.

II. EXPERIMENTATION

1. Experimental Setup and Conditions

The experiments were conducted in the Hydraulic Laboratory, Department of Civil Engineering, National Chung Hsing University, Taiwan. A glass-walled and glass-bottomed wave flume of 14 m long, 0.25 m wide and 0.5 m deep was used. The wave flume was fitted with a piston-type wave maker at one of its end, which was driven by a servo motor; while at the other end, a wave dissipator was installed to dampen waves and absorb energy. An electromagnetic clutch installed inside the wave maker allowed a rapid start and stop of the wave paddle, thereby facilitating generation of the desired solitary waves. The servo motor used to trigger the wave paddle made it possible to generate an individual solitary wave without creating dispersive tail wave train. The validations of the generated solitary wave will be discussed later. Two capacitance wave gauges located 100 cm apart were used to observe the free surface elevation and to find wave celerity using cross correlation of these two time series of the free surface elevations. In addition, an automatic system controlled by the two wave gauges was used during flow visualization and HSPIV measurements. When the free surface elevation η of a solitary wave crossing the first gauge reached 1.0 cm, a signal was sent to the high-speed camera through an amplifier and converter, and then activated the camera to start capturing images.

Flow visualization observations and HSPIV measurements were taken at a central section located 8.0 m downstream from the wave board. Two fields of view (FOV) were taken: (1) FOV A with its effective size 12.0 cm \times 12.0 cm covering the external flow field above the boundary layer, and (2) FOV B located near the bottom boundary area of 2.0 cm \times 1.0 cm with 1.0 cm of its width on either side. Fig. 1 shows a schematic view of the wave flume with the location of flow visualization and PIV measurements, two FOV's and the coordinate system

Table 1. Details of experimental conditions.

Case	Wave height	Water depth	$\frac{H}{h}$	Wave celerity	Reynolds number	Reynolds number
	H (cm)	h (cm)	$\frac{H}{h}$	c (cm/s)	R_1	R_2
A	1.3	10	0.130	104.9	1.1×10^4	4.6×10^3
B	1.2	7	0.171	90.1	8.9×10^3	4.2×10^3
C	1.5	7	0.214	90.9	1.1×10^4	5.6×10^3
D	2.1	8	0.263	98.0	1.6×10^4	8.9×10^3
E	1.9	7	0.271	93.5	1.4×10^4	8.0×10^3
F	2.9	8	0.363	102.0	1.9×10^4	1.1×10^4
G	2.7	7	0.386	99.0	1.8×10^4	1.1×10^4

used in the study. The origin of the coordinate system is located at the bottom center of FOV B with X along the bottom of the flume in the wave-motion direction, and Y normal to the bottom of the flume. The time $t = 0$ indicates the moment when the crest of the solitary wave crosses the position $X = 0$. Seven test cases were carried out with the ratio of wave height to water depth, H/h , ranging from 0.130 to 0.386.

Table 1 lists the wave condition and flow property of each tested case. The wave celerity in the table was measured value and to be compared with theoretical formula (discussed in the latter section). Two different Reynolds numbers are defined and listed in the table. The first Reynolds number is defined as $R_1 = hU/\nu$, where h represents the still water depth, U is the maximum free stream velocity at the edge of bottom boundary layer [$= (u_\infty)_{max}$] and ν denotes the kinematic viscosity of water. Herein, the length scale a of the second Reynolds number $R_2 (= aU/\nu)$ is half of the stroke of the water particle displacement in the free stream (Carstensen et al., 2010 and Sumer et al., 2010). The ranges of R_1 and R_2 in this study vary from 8.9×10^3 to 1.9×10^4 and from 4.2×10^3 to 1.1×10^4 , respectively. As pointed out by Sumer et al. (2010), the boundary layer flow experiences three kinds of flow regimes as R_2 increases: (1) laminar if $R_2 < 2 \times 10^5$; (2) laminar with vortex tube if $2 \times 10^5 < R_2 < 5 \times 10^5$; and (3) transitional if $R_2 > 5 \times 10^5$. Based on the R_2 values in the classification of Sumer et al. (2010), flow regime in the present experiments is of the laminar boundary layer.

2. Particle-Trajectory Flow Visualization Technique

The flow structure within the wave field was visualized using particle trajectory flow visualization technique. Water in the wave flume was mixed with Titanium Dioxide particles of mean diameter $1.8 \mu\text{m}$ for illumination under laser light sheet. The settling velocity (i.e., fall velocity) of a spherical titanium dioxide particles determined by Stoke's law is 4.5×10^{-4} cm/s, which is much smaller than the wave celerity c and the representative particle velocity in the present study. A 5 W argon-ion laser (Coherent Innova-90) was employed as a light source; laser beam was reflected by a glass cylinder of 0.57 cm diameter and spread into a fan-shaped light sheet of 1.5 mm thick, see Fig. 1.

The light sheet was directed upward into the flow region

through the glass bottom along the flume center line to illuminate the 2-D motion of the tracing particles. An image recording system, which is a 10-bit complementary metal-oxide semiconductor (CMOS) high-speed digital camera (Phantom V5.1) with resolution of 1024×1024 pixels and maximum framing rate of 1200 Hz, was used to capture particle-laden images of the wave field. For FOV B, which is close to the bottom boundary area, the digital camera had 1024×1024 pixel resolution, 40 Hz framing rate, and focal length 200 mm; while in the external flow field (FOV A) the camera settings were 1024×512 pixel resolution, 20 Hz framing rate, and 60 mm focal length.

3. Velocity Measurements by HSPIV

A HSPIV system was employed to measure the two-dimensional velocity field in and near the bottom boundary layer induced by a solitary wave as it propagates over the horizontal bottom. The HSPIV system consists of an argon-ion laser as light source and a high speed camera to capture the images. The laser, optics for laser-light sheeting, seeding particles, and high speed camera used for the HSPIV measurements are all the same as those used in the flow visualization tests. A Nikon 200 mm lens was mounted on the camera to allow high resolution image-capturing and adequate magnification. Before performing the cross-correlation calculation for the velocity field, the following two procedures were used for the images captured by HSPIV. Firstly, all the images were processed via the Laplacian edge-enhancement technique (Adrain and Westerweel, 2011) to intensify the brightness of the particles. Secondly, following the image-processing steps described in the hybrid digital particle-tracking velocimetry technique (Cowen and Monismith, 1997), after contrast enhancement, the images were deducted from the background images to remove any constant noise source. Velocity fields in and near the boundary layer were then determined by cross-correlation analysis. The interrogation windows of 32×32 pixels with 50% overlap were used in the analysis. Note that 15 runs of test were completed repeatedly for each experimental case. Ensemble average was then used to average the data at the same time instant in each realization. The resulting averaged horizontal velocity is hereafter termed as horizontal velocity u .

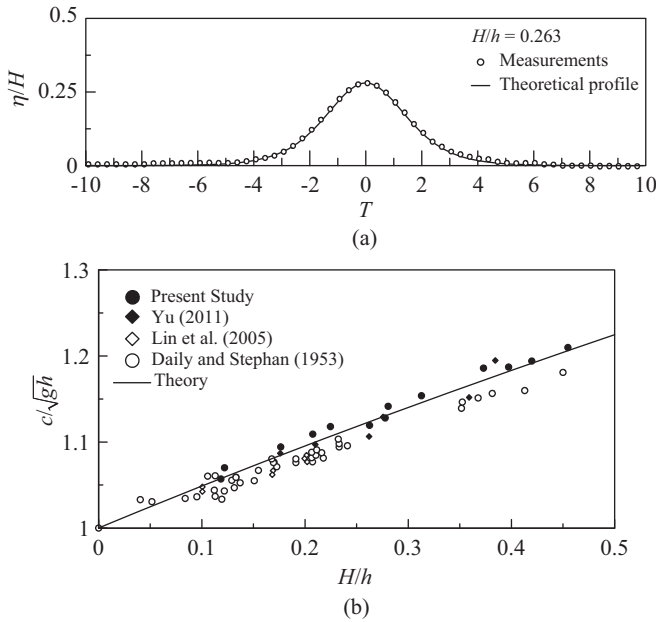


Fig. 2. (a) Free surface profile of Case D, and (b) validation of solitary wave celerity.

III. VERIFICATIONS OF WAVE PROFILE AND VELOCITY

1. Validation of Solitary Wave Generation

The wave maker was fitted with high precision servo motor system, which could generate a solitary wave nearly without dispersive tail wave train. The generated solitary waves were generated by the procedure described in Goring (1978). Along with the generated solitary wave, its wave celerity was also assessed. Fig. 2(a) presents the comparison of non-dimensional time history of the free surface elevation between the generated solitary wave and the theoretical wave profile given by

$$\eta(X,t) = H \operatorname{sech}^2 \left[\sqrt{\frac{3H}{4h^3}} (X - ct) \right] \quad (1)$$

where the wave celerity c can be obtained as $[g(H+h)]^{1/2}$. It is interesting to observe a good conformity between these two. Besides, the comparison of wave celerity is also illustrated in Fig. 2(b). Satisfactory agreements can be clearly seen between the generated waves in the present study and the data of Daily and Stephan (1953) and Lin et al. (2005, 2006).

2. Verification of Velocity Measured by HSPIV

Parallel to the HSPIV system, a fiber LDV was also used to verify the velocity measurements made by HSPIV. The LDV equipment was a two-component color burst-based, four-beam fiber-optic system (TSI System 90-3) with a 5 W argon-ion laser tube (Coherent Innova 90). Detailed descriptions of the LDV system can be referred to Lin et al. (2003, 2009). Herein,

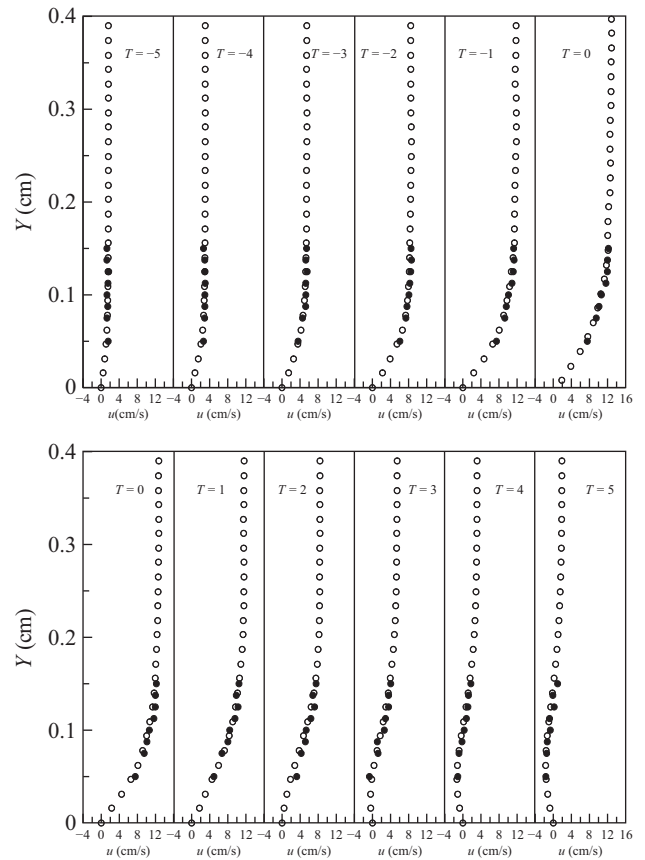


Fig. 3. Horizontal velocity profiles u of Case D measured by HSPIV (○) and LDV (●).

the non-dimensional time is defined as $T = t \times (g/h)^{1/2}$, in which t is time reflecting the phase or relative position of wave crest from the specified measuring section, and g is gravitational acceleration. Note that $T = 0$ (also $t = 0$) identifies the instant when the solitary wave crest is right passing the specified measuring section. Fig. 3 shows the comparison of the horizontal velocity profiles measured by both HSPIV and LDV for Case D at the non-dimensional time, $T = -5.00$ to $+5.00$. It can be evidenced that in the bottom boundary the LDV data collapse very well with those of the HSPIV measurements for different T , depicting satisfactory agreements between these two types of measurements. Hence, the HSPIV were considered as well acceptable in the study.

IV. RESULTS AND DISCUSSIONS

1. Flow Property and Velocity Characteristics

The images of flow visualization captured by the high-speed digital camera in FOV A during $-3.0 \leq T \leq 4.0$ are presented in Fig. 4, with the corresponding ensemble-averaged velocity fields shown in Fig. 5. From Fig. 4, it can be clearly visualized that the solitary wave approaches towards the measuring section as T tends to zero. This is also exhibited by the velocity vectors for $T = -3.0$ to -1.0 in Fig. 5. The solitary

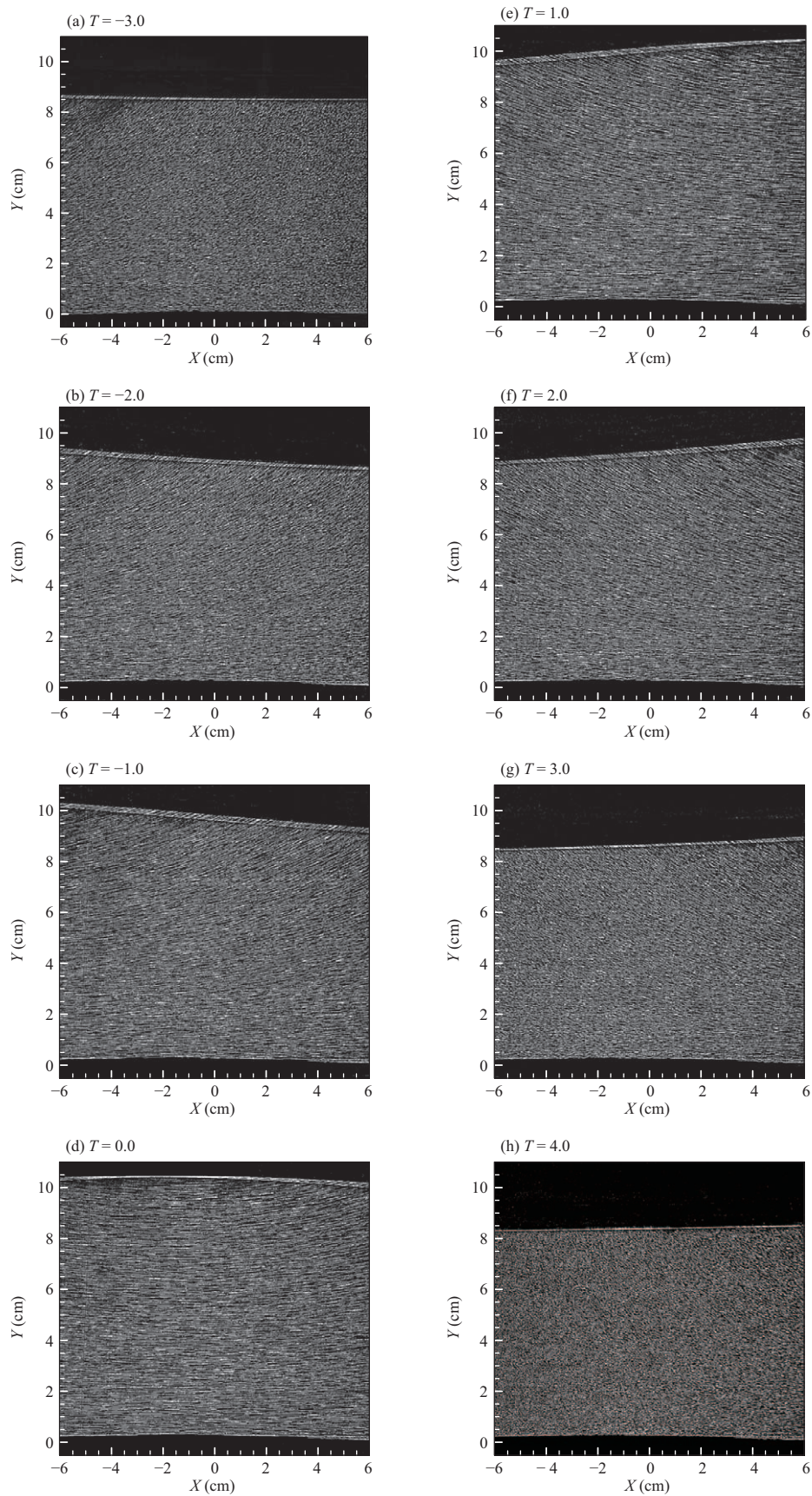


Fig. 4. Flow visualization images (FOV A) of Case D.

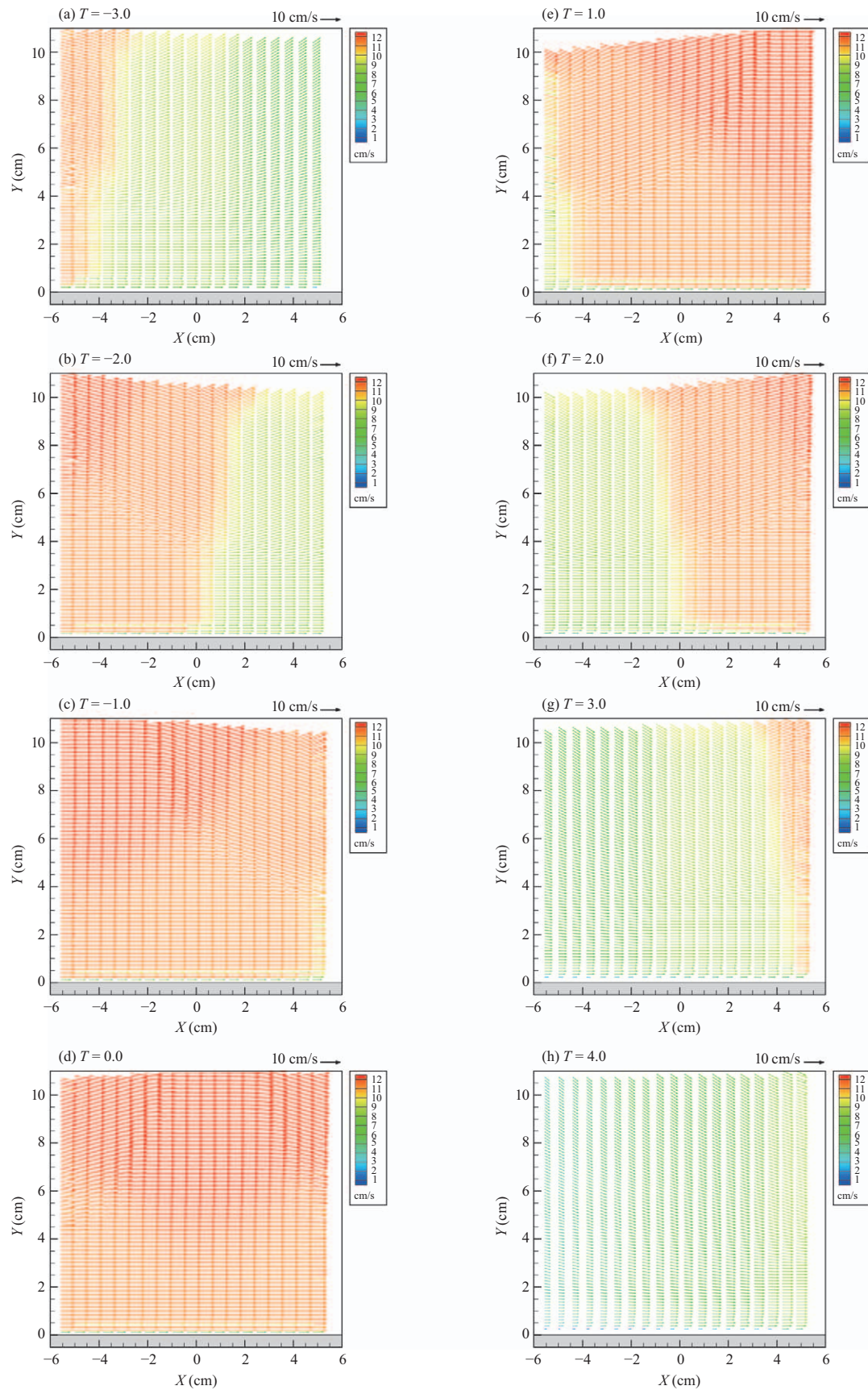


Fig. 5. HSPIV velocity fields (FOV A) of Case D.

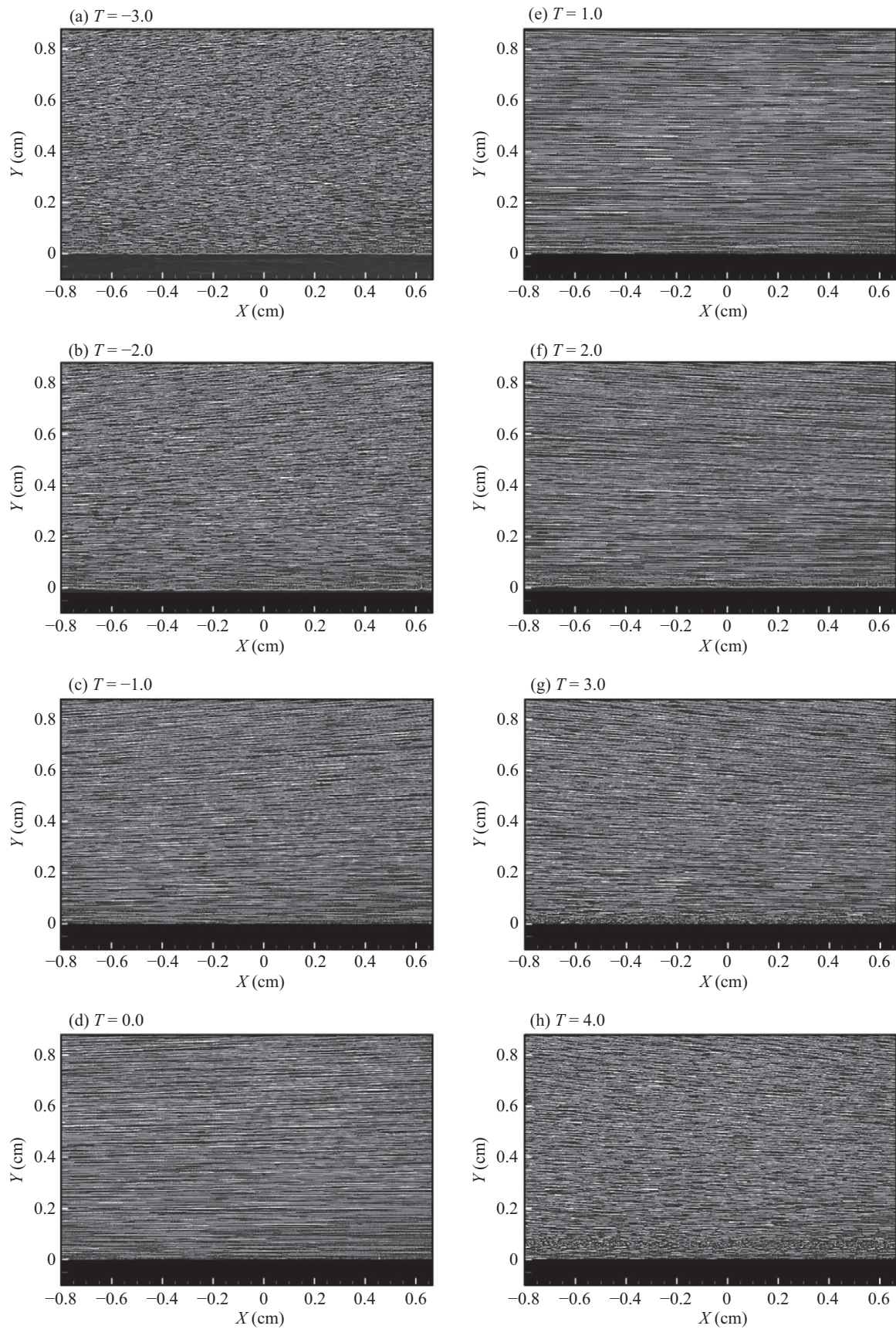


Fig. 6. Flow visualization images (FOV B) of Case D.

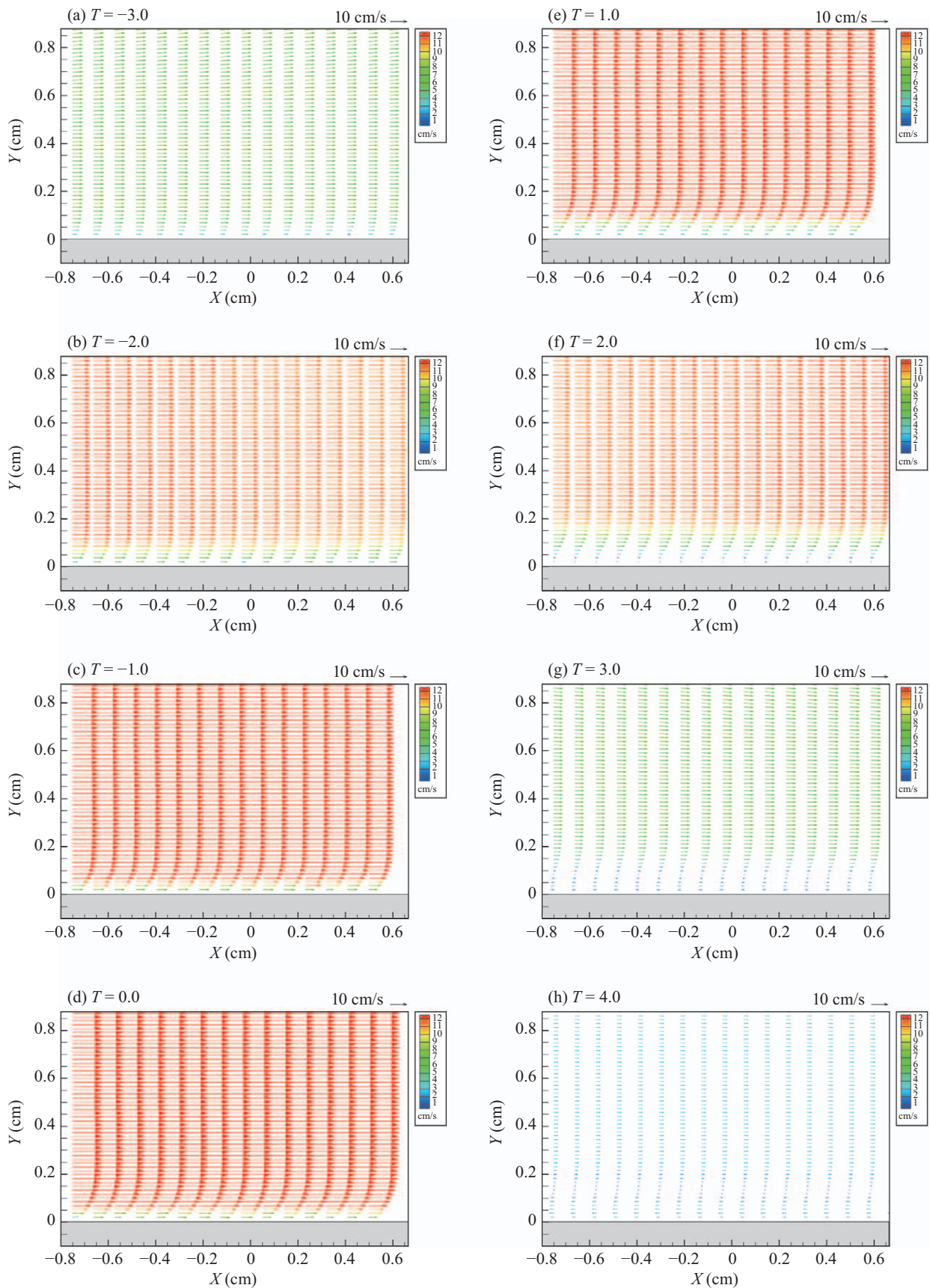


Fig. 7. HSPIV velocity fields (FOV B) of Case D.

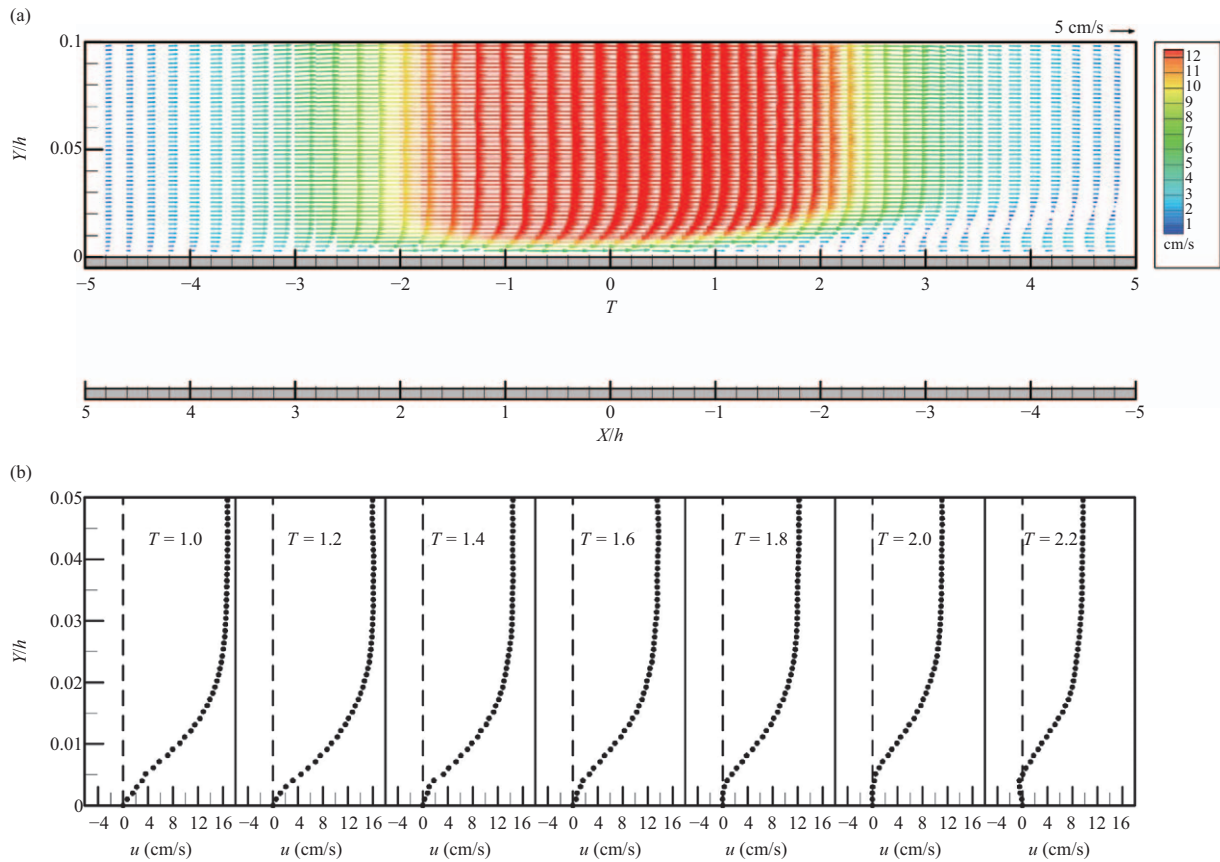


Fig. 8. (a) Temporal and spatial velocity field of Case D and (b) velocity profiles showing the occurrence of flow reversal.

wave crosses the measuring section at $T = 0$, and moves further in $T = 1.0$ to 4.0 . Note that $T = 0$ indicates the instant when the solitary wave crest reaches $X = 0$ (i.e., 8.0 m away from the wave paddle at rest). Since the boundary area was not clearly visualized in the above images, particle trajectory technique was then applied to the smaller FOV B. The resulting images and ensemble-averaged velocity fields are presented in Figs. 6 and 7.

The ensemble-averaged velocity fields in Fig. 7 exhibit uniform velocity across the depth outside the bottom boundary layer. Inside the boundary layer, the velocity decreases gradually to zero on the bottom. After $T \geq 2.0$ reversal of flow occurs near the bottom corresponding to the deceleration of the solitary wave. Liu et al. (2007) explained the rotational velocity component inside the boundary layer lags behind the irrotational velocity component outside the boundary layer due to the energy dissipation from the bottom. A negative vorticity of these two velocity couples causes flow reversal in the deceleration (post-passing) phase. The reverse flow at $T \geq 2.0$ resembles a wall jet in the opposite direction against the wave propagation, giving an indication of the development of negative or adverse pressure gradient near the bottom boundary after the passage of wave crest ($T = 0$). Fig. 8(a) plots the temporal variation of u , showing the flow reversal (reverse flow) occurs at about $T = T_{fr} = 1.8$. The close-up in Fig. 8(b)

shows how T_{fr} was determined by consecutive velocity profiles. The thickness of the reverse flow distribution increases with time after $T \geq T_{fr}$ and reaches as high as $Y/h \approx 0.025$. Fig. 8(a) also depicts another horizontal scale $5.0 \geq X/h \geq -5.0$ corresponding to the same velocity field. However, it needs to point out that the values of X/h were obtained by parametric transformation using the theoretical wave form of Eq. (1). With this X/h scale, it could be identified that the starting point where the reverse flow occurs is at about $X = -1.8h$ from the measuring section.

After obtaining the non-dimensional time T_{fr} and position X_{fr}/h defined as the occurrence of reverse flow, their variations in different relative wave height H/h are plotted in Fig. 9. It shows that both T_{fr} and X_{fr}/h have linear relationships with H/h ; while T_{fr} decreases with an increase in H/h , X_{fr}/h increases with it. A greater H/h generates larger negative pressure gradient, thus expediting the occurrence of reverse flow and moving its occurring position closer to the measuring section. The resulting regression equations are

$$T_{fr} = -1.79 \frac{H}{h} + 2.32 \quad (2)$$

$$\frac{X_{fr}}{h} = 2.37 \frac{H}{h} - 2.72 \quad (3)$$

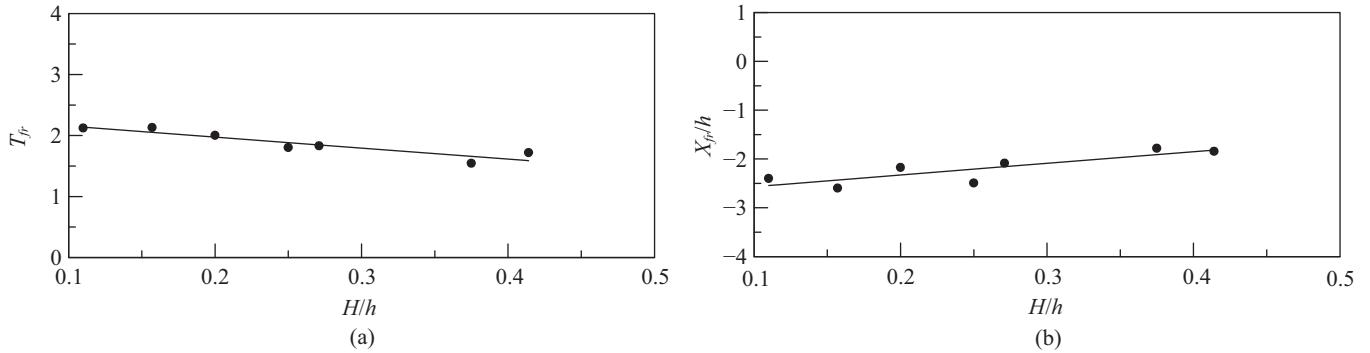


Fig. 9. Occurrence of reverse flow versus H/h : (a) T_{fr} and (b) X_{fr}/h .

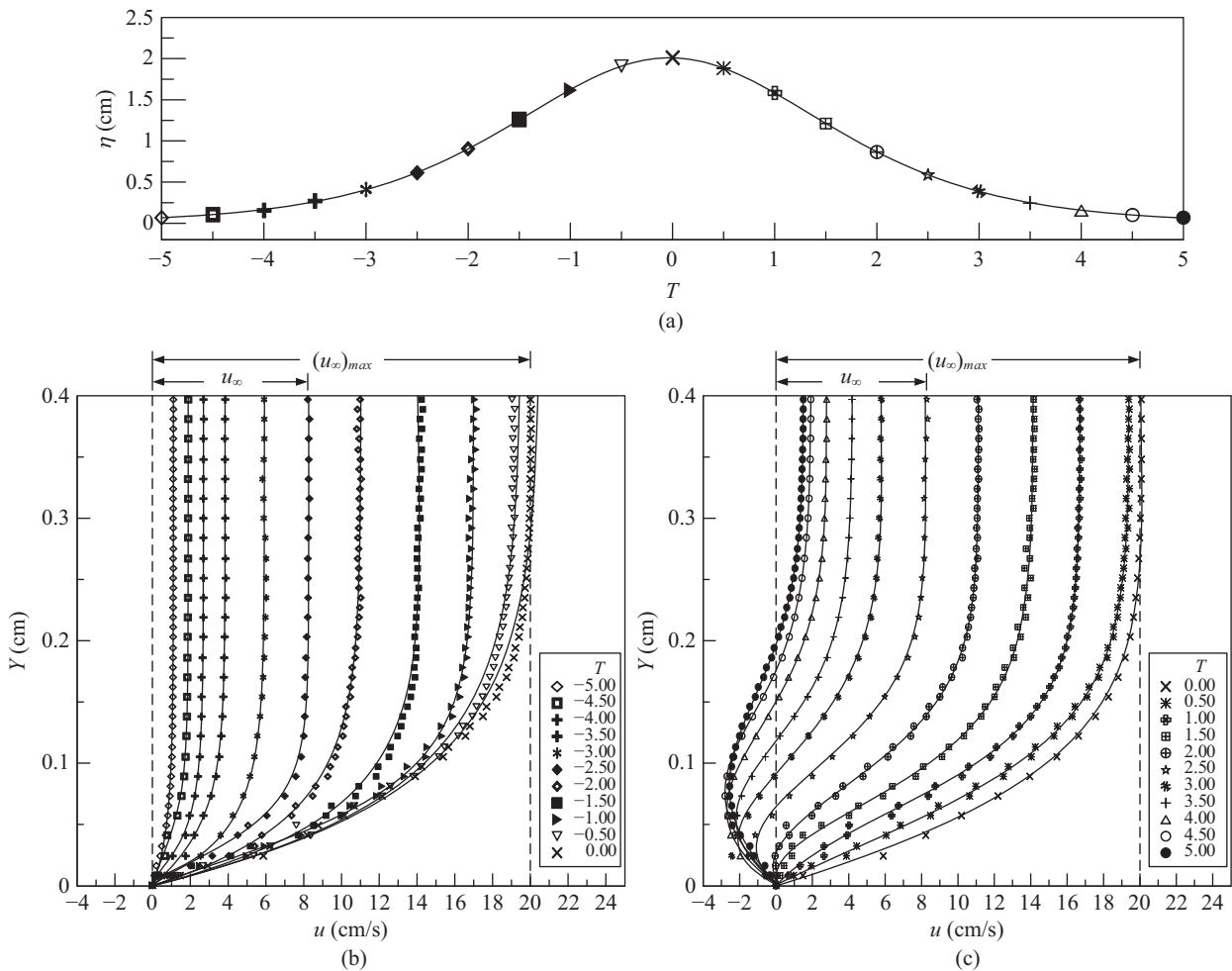


Fig. 10. Velocity profiles of Case D: (a) measuring instants, (b) pre-passing phase and (c) post-passing phase.

The velocity profiles of the (ensemble-averaged) horizontal velocity u for Case D with $-5.0 \leq T \leq 5.0$ at every $\Delta T = 0.5$ is presented in Fig. 10. It is interesting to observe that the profiles follow certain pattern for every T independently, and can be in the prepassing phase, u increases with distance to the bottom boundary; its magnitude starts from zero, gradually increases and finally reaches the free stream velocity u_∞ at the

edge of the boundary layer thickness δ . A schematic diagram of the velocity profile is sketched in Fig. 11(a). The distance and magnitude of u_∞ both increase with the approaching of the solitary wave from $Y = 0.10$ cm and $u = 1.2$ cm/s at $T = -5.0$ to $Y = 0.25$ cm and $u = 20.0$ cm/s at $T = 0$. The maximum free stream velocity at $T = 0$ is particularly denoted as $(u_\infty)_{max}$.

On the other hand, the u profiles remain the same shapes as

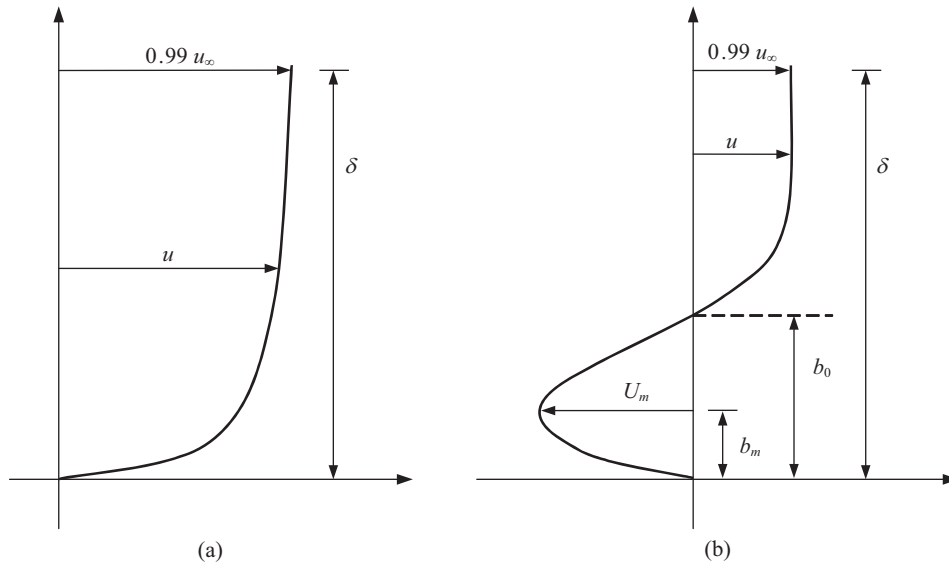


Fig. 11. Schematic diagrams of characteristic profiles of u : (a) pre-passing phase ($T \leq 0.0$), and (b) post-passing phase ($T \geq 0.0$) including the reverse flow.

in the pre-passing phase, but u_∞ starts to decrease with increase in T in the beginning of the post-passing phase. After some time steps ($T = 1.8$ in Case D), a portion on the profile from the bottom boundary undergoes flow reversal, in which u is in the negative direction. The magnitude of u starts from zero at the boundary and increases (in negative) with distance from the bottom. The velocity reaches its negative maximum $U_m (< 0)$ at a distance $Y = b_m$ and starts to decrease (in positive) with further distance away from the boundary. After turning back to zero at $Y = b_0$, u continues to increase until reaching u_∞ in the free stream. A typical velocity profile in the post-passing phase including the reverse flow is depicted in Fig. 11(b). It is pertinent to mention that u_∞ continues to decrease with increase in T in the post-passing phase. The velocity profile of the reverse flow is very similar to a wall jet; its thickness (i.e., b_0) and the height of U_m (i.e., b_m) both increase with T , but the magnitude of U_m has its negative maximum value $(U_m)_{max}$ at a specific time $T = (T)_{max}$. In Case D, $(U_m)_{max} = -3.1$ cm/s at $b_m = (b_m)_{max} = 0.11$ cm when $(T)_{max} = 4.3$. The corresponding thickness of the reverse flow [$b_0 = (b_0)_{max}$] is about 0.21 cm.

2. Analysis of Similarity Profile

The nonlinear regression analysis was performed to the measured u profiles according to the two phases defined earlier. To obtain the fitting curves for the velocity profiles in the pre-passing phase, a nonlinear regression equation with two hyperbolic tangent functions was considered.

$$u(Y) = C_1 \tanh(C_2 Y + C_3) \tanh(C_4 Y + C_5) + C_6 \quad (4)$$

where C_1 to C_6 are regression constants and available in Yu (2008). Curve fitting of this equation to all measured velocity profiles gives a R^2 value of 0.993, and the fitted velocity pro-

files are plotted as solid lines in Fig. 10(b). In the post-passing phase, two characteristic length scales (b_m and b_0) exist in the velocity profile when the reverse flow reaches its negative maximum ($U_m = (U_m)_{max}$) as shown in Fig. 11(b). Note that far beyond the flow reversal zone, u also reaches asymptotically the free stream velocity u_∞ at $Y = \delta$. To match this specific nature, a nonlinear regression equation consisting of a hyperbolic tangent function and a cosine function was selected

$$u(Y) = C_7 [\tanh(C_8 Y + C_9) - 1] \cos(C_{10} Y + C_{11}) + C_{12} \quad (5)$$

where C_7 to C_{12} are regression constants (also given in Yu, 2008). The fitted velocity profiles illustrated as solid lines in Fig. 10(c) demonstrate good agreements with the measurements.

The results were further compiled together to obtain velocity similarity profiles for the two phases. In the pre-passing phase, the boundary layer thickness δ and the free stream velocity u_∞ were chosen as length and velocity scales, respectively. Fig. 12 shows the novel similarity profile, which can be expressed as

$$\frac{u}{u_\infty} = 1 - e^{-4.29 Y / \delta} \quad (6)$$

Even though flow within the bottom boundary layer due to propagation of a solitary wave is a best example of unsteady flow, the present investigation demonstrates that the characteristics of boundary layer still equivalently follow normal steady flow conditions. Hence, the flow fields in the pre-passing phases exhibit as the traditional laminar boundary layer flow over a flat plate.

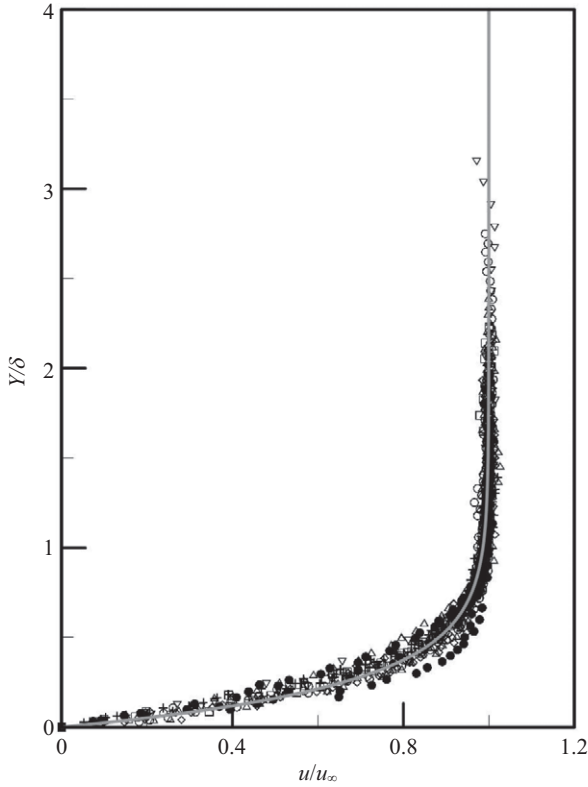


Fig. 12. Similarity profile of u in the pre-passing phase: (+) Case A, (\diamond) Case B, (Δ) Case C, (\bullet) Case D, (\circ) Case E, (\square) Case F, (∇) Case G, and (—) similarity profiles.

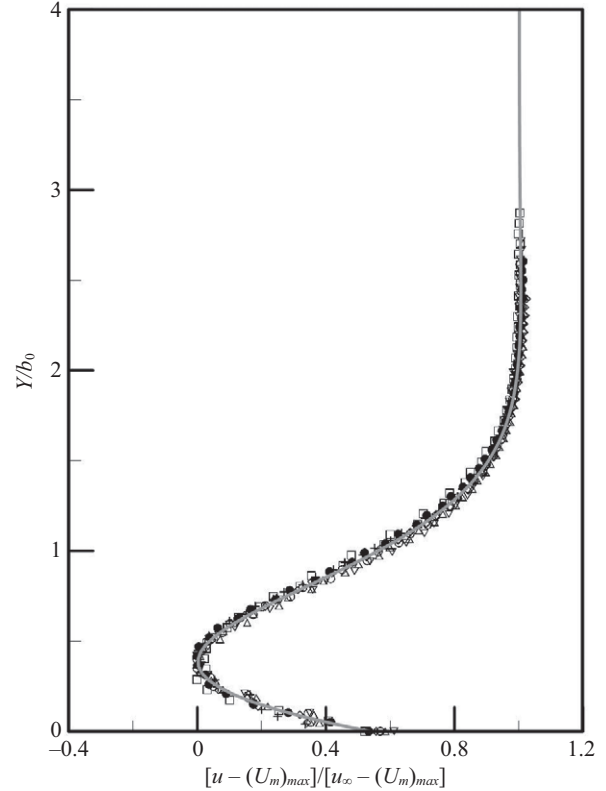


Fig. 13. Similarity profile of u in the post-passing phase based on $(U_m)_{max}$. For symbols, see Fig. 12.

Similarly, a striking similarity profile of u was obtained for the post-passing phase. Since the variation of velocity profile is far more complex due to the occurrence of reverse flow, only those specific profiles of negative maximum velocity of flow reversal were considered, i.e., $U_m = (U_m)_{max}$, when $T = (T)_{max}$. Note that the corresponding time and length scales of this profile are denoted as $(T)_{max}$, $(b_m)_{max}$, and $(b_0)_{max}$, respectively.

Fig. 13 shows very good self-similarity of the velocity measurements and a fitting curve with R^2 value of 0.998 results in Eq. (7).

$$\frac{u - (U_m)_{max}}{u_\infty - (U_m)_{max}} = \left[-1.78 \tanh\left(1.33 \frac{Y}{(b_0)_{max}} - 0.35\right) + 1.78 \right] \times \cos\left(-1.40 \frac{Y}{(b_0)_{max}} - 1.77\right) + 1.00 \quad (7)$$

along with the free stream velocity u_∞ as the *characteristic velocity scale*. Note that $(T)_{max}$, $(U_m)_{max}$ and $(b_0)_{max}$ in this equation are all linearly related to H/h (see Fig. 14) as

$$(T)_{max} = -7.58 \frac{H}{h} + 6.64 \quad (8a)$$

$$\frac{(U_m)_{max}}{\sqrt{gh}} = -0.08 \frac{H}{h} - 0.01 \quad (8b)$$

$$\frac{(b_0)_{max}}{H} = -0.44 \frac{H}{h} + 0.21 \quad (8c)$$

V. CONCLUSIONS

The characteristics of boundary layer flow induced by a solitary wave propagating over a horizontal bottom have been investigated, using particle trajectory technique and HSPIV. Some important results are summarized as follows:

1. Based on the nature of horizontal velocity profile in the bottom boundary layer, its characteristics can be classified into two phases according to the passage of the solitary wave crest: the pre-passing phase and the post-passing phase. In the pre-passing phase, the velocity distribution in the unsteady boundary layer is similar to the traditional laminar boundary layer flow over a flat plate, while in the post-passing phase, flow reversal behaving occurs, resulting in the deceleration of wave.
2. The reverse flow resembles a wall jet in the opposite direction against the wave propagation, giving an indication

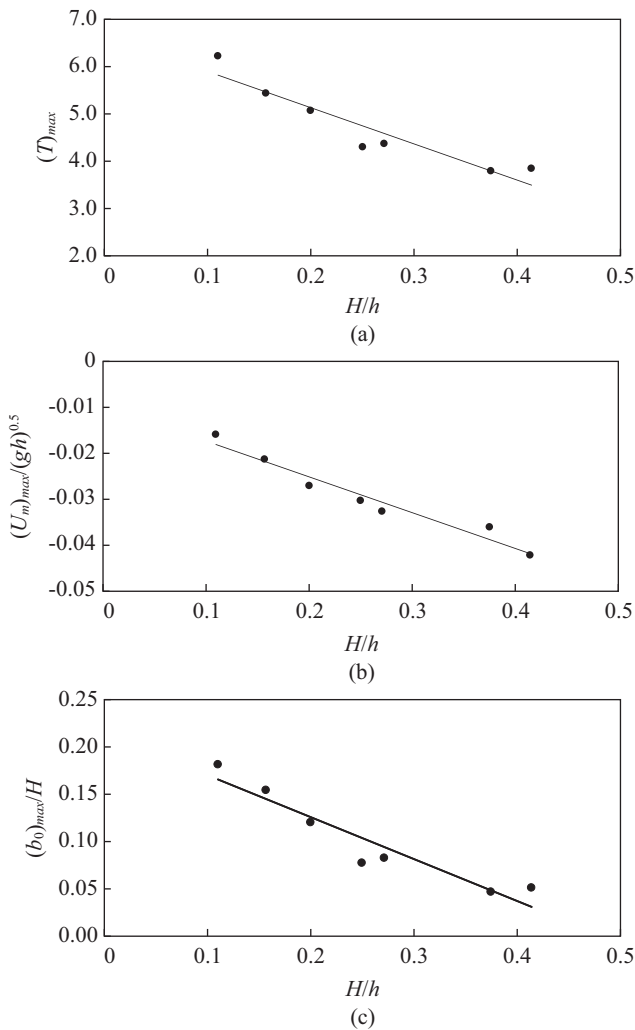


Fig. 14. (a) $(T)_{max}$, (b) $(U_m)_{max}$ and (c) $(b_0)_{max}$ versus H/h . (•) measurements, (—) regression equations.

of the development of negative or adverse pressure gradient near the boundary. Its occurring time and position both have linear relationships with the relative wave height of solitary wave; while the occurring time decreases with an increase in relative wave height, the occurring position increases with it. A greater ratio of wave height to water depth generates larger negative pressure gradient, thus expediting the occurrence of the reverse flow and moving its occurring position closer to the measuring section.

3. A regression equation with two hyperbolic tangent functions was used as anticipated velocity distribution in the bottom boundary layer and curve-fitted with the measurement data in the pre-passing phase. The results were further compiled together to get the velocity similarity profile [Eq. (6)]. The free stream velocity and the boundary layer thickness were used as the velocity and length scales, respectively.
4. On the other hand, velocity distributions in the post-passing phase were curve-fitted by an equation consisting of a hy-

perbolic tangent and a cosine function. Due to the complexity of the flow field, a similarity profile [Eq. (7)] was obtained for the profiles with a negative maximum velocity. The velocity deficit between the unsteady free stream velocity and the maximum negative velocity as well as the (time-dependent) thickness of reversal flow were identified as the characteristic velocity and length scales, respectively.

ACKNOWLEDGMENTS

This work was performed under the support of National Science Council, Taiwan (Grant No. NSC 99-2221-E-005-117-MY3). The authors would like to express their sincere appreciation to UTOPIA Instruments Co., Ltd. for helping the test of high-speed digital camera.

REFERENCES

- Adrain, R. J. and J. Westerweel (2011). Particle Image Velocimetry. Cambridge University Press, New York.
- Carstensen, S., B. M. Sumer and J. Fredsøe (2010). Coherent structures in wave boundary layers. Part 1. Oscillatory motion. *Journal of Fluid Mechanics* 646, 169-206.
- Chang, C. H., C. J. Tang and C. Lin (2012). Vortex generation and flow pattern development after a solitary wave passing over a bottom cavity. *Computer and Fluid* 53, 79-92.
- Cowen, E. A. and S. G. Monismith (1997). A hybrid digital particle tracking velocimetry technique. *Experiments in Fluids* 22, 199-211.
- Daily, J. W. and S. C. Stephan (1953). Characteristics of the solitary wave. *Transactions of the American Society of Civil Engineers* 118, 575-587.
- Goring, D. G. (1978). Tsunamis—the propagation of long waves onto a shelf, Ph.D. Dissertation, California Institute of Technology, Pasadena, California.
- Jensen, B. L., B. M. Sumer and J. Fredsøe (1989). Turbulent oscillatory boundary-layers at high Reynolds-numbers. *Journal of Fluid Mechanics* 206, 265-297.
- Keulegan, G. H. (1948). Gradual damping of solitary wave. *Journal of Research of the National Bureau of Standards* 40, 487-498.
- Lin, C., S. C. Chang, T. C. Ho and K. A. Chang (2006). Laboratory observation of a solitary wave propagating over a submerged rectangular dike. *Journal of Engineering Mechanics* 132, 545-554.
- Lin, C., T. C. Ho, S. C. Chang, S. C. Hsieh and K. A. Chang (2005). Vortex shedding induced by a solitary wave propagating over a submerged vertical plate. *International Journal of Heat and Fluid Flow* 26, 894-904.
- Lin, C. and H. H. Hwung (2002a). Observation and measurement of the bottom boundary layer flow in the pre-breaking zone of shoaling waves. *Ocean Engineering* 29(12), 1479-1502.
- Lin, C., C. N. Jeng, D. S. Jeng and C. P. Tsai (2002b). Characteristics of flow field in potential region of finite amplitude standing waves. *Journal of Engineering* 13(3), 181-200.
- Lin, C., D. S. Jeng and C. N. Jeng (2002c). An experimental study on flow characteristics of standing wave: Application of FLDV measurements. *Ocean Engineering* 29(10), 1265-1282.
- Lin, C., W. J. Lai, and K. A. Chang (2003). Simultaneous PIV and LDV measurements of periodical oscillatory horseshoe vortex system near square cylinder-base plate juncture. *Journal of Engineering Mechanics* 129(10), 1173-1188.
- Lin, C., W. J. Lin, S. C. Hsieh, S. S. Lin and S. Dey (2009). Flow characteristics around a circular cylinder placed horizontally above a plane boundary. *Journal of Engineering Mechanics* 135(7), 697-716.
- Lin, C., P. H. Yeh, S. C. Hsieh, Y. N. Shih, L. F. Lo and C. P. Tsai (2014a). Pre-breaking internal velocity field induced by a solitary wave propagating over a 1:10 slope. *Ocean Engineering* 80, 1-12.

- Lin, C., P. H. Yeh, M. J. Kao, M. H. Yu, S. C. Hsieh, S. C. Chang, T. R. Wu and C. P. Tsai (2014b). Velocity fields inside near-bottom and boundary layer flow in pre-breaking zone of solitary wave propagating over a 1:10 slope. *Journal of Waterways, Port, Coastal, and Ocean Engineering*, ASCE.
- Liu, P. L.-F. (2006). Turbulent boundary-layer effects on transient wave propagation in shallow water. *Proceedings of the Royal Society A* 462, 3481-3491.
- Liu, P. L.-F. and A. Orfila (2004). Viscous effects on transient long-wave propagation. *Journal of Fluid Mechanics* 520, 83-92.
- Liu, P. L.-F., G. Simarro, J. Vandever and A. Orfila (2006). Experimental and numerical investigation of viscous effects on solitary wave propagation in a wave tank. *Coastal Engineering* 53, 181-190.
- Liu, P. L.-F., Y. S. Park and E. A. Cowen (2007). Boundary layer flow and bed shear stress under a solitary wave. *Journal of Fluid Mechanics* 574, 449-463.
- Mei, C. C. (1983). *The Applied Dynamics of Ocean Surface Waves*, 2nd Ed., John Wiley and Sons.
- Ott, E. and R. N. Sudan (1970). Damping of solitary waves. *Physics of Fluids* 13(6), 1432-1434.
- Sleath, J. F. A. (1987). Turbulent oscillatory flow over rough beds. *Journal of Fluid Mechanics* 182, 369-409.
- Sumer, B. M., P. M. Jensen, L. B. Sørensen, J. Fredsøe, P. L.-F. Liu and S. Carstensen (2010). Coherent structures in wave boundary layers-- Part 2. Solitary motion. *Journal of Fluid Mechanics* 646, 207-231.
- Yu, S. M. (2008). The characteristics of bottom boundary layer flow induced by solitary wave. Master Thesis, National Chung Hsing University, Taiwan. (in Chinese)
- Yu, M. H. (2011). Study on the characteristics of bottom boundary layer flow induced by a solitary wave propagating over a sloping bottom. Master Thesis, National Chung Hsing University Taiwan. (in Chinese)